Journal of Computational Physics 513 (2024) 113186

Contents lists available at ScienceDirect

Journal of Computational Physics

journal homepage: www.elsevier.com/locate/jcp

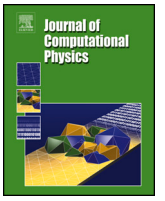

A single mesh approximation for modeling multiphase flow in heterogeneous porous media

Jumanah Al Kubaisy [a,*], Pablo Salinas [b], Matthew D. Jackson [a]

[a] Novel Reservoir Modelling and Simulation Group, Department of Earth Science and Engineering, Imperial College London, Exhibition Road, London, SW7 2AZ, UK

[b] OpenGoSim Ltd, 30 Nelson Street, Leicester, LE1 7BA, UK

ARTICLE INFO

Keywords:
CVFE methods
Multiphase flow
Low order method
Discontinuous Galerkin
Discontinuous pressure formulation
Complex geometry

ABSTRACT

The control volume finite element (CVFE) approach is based on the discretization of primary flow and transport unknowns on two different meshes. The element mesh, used to represent the physical properties of the medium, differs from the control volume mesh necessary to ensure a mass conservative solution. The inherent two mesh feature of the CVFE approximation introduces inconsistency in the transport solution due to the averaging of physical and computed quantities between neighboring elements in the mesh. In this work, we present a consistent approach for modeling multiphase flow and transport in heterogeneous porous media. The approach is applied in the CVFE framework by enabling the discretization of primary unknowns on a single mesh. We combine the discretization of an element-wise, discontinuous pressure approximation with a first-order, discontinuous velocity approximation to resolve the elliptic or parabolic flow problem. The effectiveness of the formulation is achieved by exploiting the same finite element mesh as the flow problem, when updating the saturation solution. This direct mapping between the flow and transport mesh is simple yet effective for establishing a consistent solution in addition to circumventing the non-physical mass leakage exhibited in the classical CVFE method. We describe the interface approximations and the discontinuous terms needed for consistent solutions. The method is well suited to model flow in complex geometrical subsurface domains and is shown to be numerically stable while providing locally and globally mass conservative solutions. We apply the approach to several domains with complex geometrical features to emphasize the superiority of the approximation over conventional methods. The analysis shows over two orders of magnitude reduction in solution error compared to the classical CVFE. The new formulation effectively captures accurate transport solutions, even in the presence of varying material properties, without the need for mesh refinement.

1. Introduction

Numerical modeling of subsurface processes plays a vital role in many applications concerning the management strategies for groundwater, energy and other natural resources, as well as contaminant remediation techniques. To accurately and effectively resolve flow dynamics in subsurface models, there has been an increasing interest in realistic material representations that capture

* Corresponding author.
E-mail addresses: j.al-kubaisy19@imperial.ac.uk, jalkubaisy@gmail.com (J. Al Kubaisy), pablo.salinas@opengosim.com (P. Salinas), m.d.jackson@imperial.ac.uk (M.D. Jackson).

https://doi.org/10.1016/j.jcp.2024.113186
Received 29 September 2023; Received in revised form 22 May 2024; Accepted 5 June 2024

Available online 10 June 2024

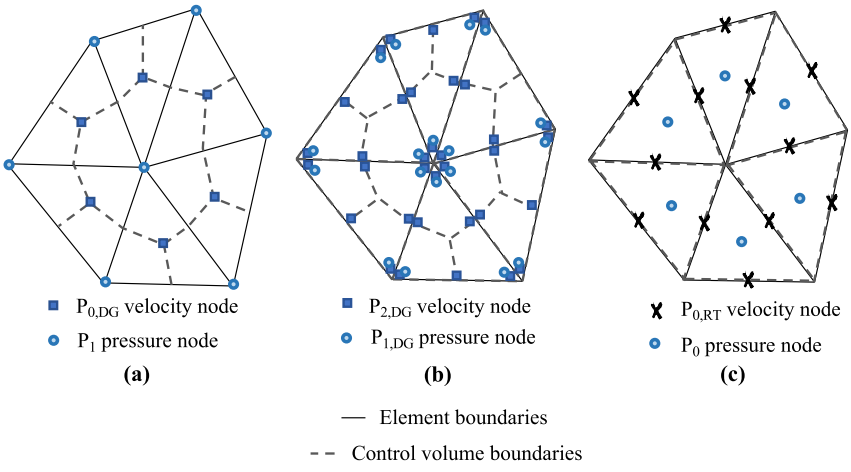

Fig. 1. Different approaches for discretizing the flow variables: (**a**) The two mesh approach used in the classical CVFE method ($P_{0,DG} - P_1$). (**b**) The two mesh approach from Salinas et al. [43] ($P_{2DG} - P_{1DG}$). (**c**) The single mesh approach used in the mixed finite element method.

the underlying heterogeneities (e.g. [30,17,24]); examples include faults, facies transitions, layering, or the presence of fractures [39,37,36]. The spatial variability of heterogeneous features often introduces multi-scale effects, locally or regionally, into the physical problem with scales spanning from millimeters to kilometers [26,22,36].

The finite element (FE) method presents a flexible approach to model flow in complex geometries. The flexibility of the method stems from decomposing the computational domain into elements that may be structured or unstructured. The flow field is then approximated by two independent variables, pressure and velocity, based on different spaces that must satisfy the inf-sup stability condition [8,9]. The flux approximation is determined by the continuity of the velocity space between volumes, or elements, within which mass is conserved. The flexible FE flow model is often combined with the stable, mass conservative finite volume (FV) approach to resolve the transport model.

When modeling flow and transport with the control volume finite element (CVFE) method, two meshes are used to capture the coupled problem [21,18,19,25,6,20,22,37,44,31,23,43]. The finite element mesh represents element-wise the petrophysical properties of the medium such as permeability and porosity. The control volume (CV) mesh is constructed around the vertices of the elements and is necessary to achieve a mass conservative transport solution. The discretization of primary flow unknowns on the two meshes for the classical CVFE method is shown in Fig. 1a. This example shows the element pair $P_{0,DG} - P_1$ that represents an element-wise, discontinuous velocity approximation combined with a Lagrangian first order pressure approximation. The element-wise approximation of velocity ensures that the fluxes are continuous within each element, including the control volume boundaries [22]. The drawback of having two meshes in the CVFE approach is that it introduces an inconsistency into the saturation solution because of the averaging between neighboring elements [43,40]. The issue is exacerbated for CV's constructed along the interfaces between model subdomains with contrasting material properties [43].

Several studies devoted to addressing the challenge of preserving material property contrasts in the CVFE method have proposed different discretization approaches of the flow unknowns [2,43,4,40,47]. One notable approach that, despite employing two meshes, accurately captures material property contrasts is that of Salinas et al. [43]. The approximation is denoted by $P_{2DG} - P_{1DG}$ which represents a second order discontinuous velocity and a first order discontinuous pressure approximation, respectively. Each element is discretized into 3 control volumes (Fig. 1b). Due to the higher order discontinuous approximation of velocity and pressure, the method requires 18 degrees of freedom (DoF) for each triangular element in 2D which is computationally very expensive. More recently, the Hybrid CVFE (HyCVFE) approach was developed to accurately and efficiently capture solutions for multiphase flow in subdomains that are internally homogeneous but have contrasting material properties [4]. For example, in a multi-layer system, each layer constitutes a homogeneous subdomain. The HyCVFE approach combines the continuous pressure approximation in each subdomain for efficiency, with a discontinuous pressure approximation applied exclusively across elements at the boundaries between subdomains. The method accurately captures the transport solution and introduces an insignificant computational overhead in terms of the total degrees of freedom. The HyCVFE approximation was designed to model multiphase flow through subdomains with contrasting material properties and does not address the general inconsistency of the dual mesh approach in the classical CVFE method.

Another approach for solving the coupled problem is based on combining the mixed finite element (MFE) method and the finite volume (FV) method. It provides a consistent approximation for coupled flow and transport on the same mesh [12,13,18,7]. The MFE and FV method employs an element-wise representation for the material properties as well as the pressure, the saturation, and the saturation dependent properties, while the velocity is established between elements using the lowest-order Raviart-Thomas (RT) approximation (Fig. 1c). The MFE approach requires more degrees of freedom compared to the classical CVFE method [19,22]. One limitation associated with the method is the indefinite linear system assembled by the MFE discretization [19]. The mixed hybrid finite element (MHFE) method has addressed the issue by introducing a trace variable on the edges between elements [14]. Later work by Hoteit et al. [28] showed that the MHFE method yields non-monotonic solutions which was then addressed by Younes et al. [49].

The mimetic finite difference (MFD) method, a relevant development to the MFE methods, emerged to handle coupled processes in complex domains [35]. More specifically, the numerical evaluation of its basis function enables the approximation of essentially any polygonal shape [3]. Recent developments of the MFD approach have been tested in different applications [41,35,50,51,3,38].

This paper introduces a new formulation that eliminates the dual mesh from the CVFE method. It is a generalization of the technique used for embedding the discontinuous Galerkin approximation in the HyCVFE approach [4]. Instead of capturing solution discontinuities only between model subdomains, we employ a new discontinuous element type that captures element to element variations in the material properties and the corresponding solution fields. The method addresses the general inconsistency described earlier of CVFE methods for modeling multiphase porous media flow. The main contributions of this work are three-fold:

1. The proposed new CVFE method employs a single mesh that ensures consistency of the flow and transport problems. Solutions are stable and mass-conservative.
2. A new element type is introduced for the discretization of velocity and pressure that allows application of the discontinuous Galerkin approximation globally in the domain. The derivation of the approach is non-trivial and is described accordingly.
3. Geo-statistical models with element-to-element variations in material properties can be modeled accurately using the proposed method.

In this paper, we present the formulation of this new single-mesh control volume finite element (SM-CVFE) method. In section 2, we review the classical governing equations of porous media flow and transport. This is followed by an introduction of the new element, the discretization of the SM-CVFE approach, and the solution method implementation in section 3. Section 4 validates the approach for single and two phase flow, then tests a variety of challenging problems that include domains with complex geometries and geo-statistical models. Finally, sections 5 and 6 provide general discussion and conclusions, respectively.

2. Governing equations

Fluid flow through porous media is described by Darcy's law, given by

$$\mathbf{v_t} = -\lambda_t \mathbf{K} \cdot \nabla p, \tag{1}$$

$\mathbf{v_t}$ is the total fluid Darcy velocity, λ_t is the total mobility, $\mathbf{K}$ is the permeability tensor, and ∇p is the pressure gradient. The gravity and capillary forces (P_c) are neglected here. Therefore, both fluid phases have the same pressure at any given location in the domain. The total mobility (λ_t) is defined as the summation of the individual phase mobility terms. The mobility of phase α is

$$\lambda_\alpha = \frac{k_{r\alpha}}{\mu_\alpha}, \tag{2}$$

where k_r and μ are the relative permeability and the dynamic viscosity, respectively. For an incompressible flow, the continuity equation is

$$\nabla \cdot \mathbf{v_t} = q_t, \tag{3}$$

where q_t denotes the source term. The fractional flow of phase α, f_α, is

$$f_\alpha = \frac{\lambda_\alpha}{\lambda_t}. \tag{4}$$

The mass balance equation of phase α is

$$\phi \frac{\partial S_\alpha}{\partial t} + \nabla \cdot (f_\alpha \mathbf{v_t}) = q_\alpha, \tag{5}$$

assuming all phases are immiscible and incompressible. Here, ϕ, t, and q denote the porosity of the medium, time, and the phase source term, respectively. The mass balance equation is expressed with the fractional flow term (f_α). We solve for the saturation unknown subject to the constraint

$$S_w + S_{nw} = 1, \tag{6}$$

for the total volume fraction. The subscripts w and nw refer to the wetting phase and non-wetting phase, respectively.

3. Method

3.1. New element representation

The SM-CVFE approach introduces a new, fully discontinuous element pair ($P_{1,DG} - P_{0,DG}$) which represents a first order discontinuous Galerkin velocity approximation combined with an element-wise, discontinuous Galerkin pressure approximation, respectively, (Fig. 2). Unlike the classical CVFE method, in the SM-CVFE method the physical properties of the medium (permeability and porosity), the pressure, the saturation and the saturation dependent properties are represented constant element-wise

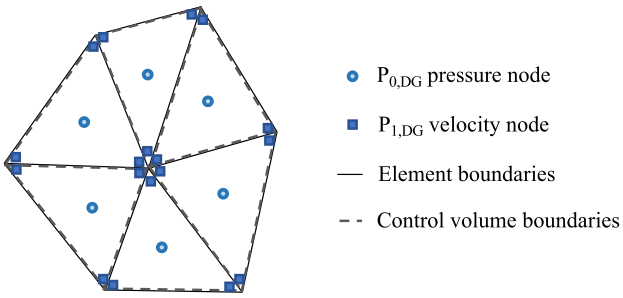

Fig. 2. The new element pair discretization used in the SM-CVFE method.

for consistency. Despite the use of a discontinuous velocity approximation between control volumes (or elements), the discretization described in the next section constructs globally continuous fluxes between control volumes. We employ the finite element method to resolve the flow problem following the CVFE approach (e.g. [19,22,31,23,43,4]). Consider the domain ($\Omega \in \mathbb{R}^2$) triangulated into N_e elements with a constrained conforming Delaunay triangulation [45]. The finite element approximation of the total Darcy velocity ($\mathbf{v_t}$) is

$$\mathbf{v_t}(\mathbf{x}) = \sum_{j \in \Omega} \mathbf{\Phi}_j(\mathbf{x}) v_{t,j}, \tag{7}$$

where $\mathbf{\Phi}(\mathbf{x})$ denotes the linear basis function of the velocity and v_t is the velocity unknown coefficient. The pressure (p) is determined by

$$p = \sum_{j \in \Omega} \Psi_j p_j, \tag{8}$$

where Ψ_j is the pressure basis function that is 1 for element j and vanishes elsewhere and p_j is the pressure unknown coefficient. This approximation employs a discontinuous space for the pressure that varies element-wise.

It is worth remarking that the SM-CVFE element approximation described by this work differs from the MFE and the approach of Salinas et al. [43]. In the MFE method, the velocity is approximated using an RT-0 element. The Salinas et al. [43] approach uses two meshes; an element mesh and a control volume mesh as shown in Fig. 1b, and therefore requires higher order approximations for both flow variables, described by $P_{2,DG} - P_{1,DG}$.

3.2. Discretization of Darcy's equation

We capture the weak form of Darcy's equation by multiplying with $\mathbf{\Phi_i}$, a test function from the velocity basis function space. Then we integrate over the computational domain (Ω)

$$\int_{\Omega} \mathbf{\Phi_i} \cdot \mathbf{v}_t \, d\Omega + \int_{\Omega} \mathbf{\Phi_i} \cdot \left(\lambda_t \mathbf{K} \cdot \nabla p \right) d\Omega = 0. \tag{9}$$

The following steps are essential to incorporate the discontinuous Galerkin pressure approximation globally in the domain. We decompose the domain using the triangulation ($\mathcal{T} = \cup_{e=1}^{N_e} \Omega_e$) where N_e is the total count of elements and Ω_e is the element domain. To accommodate for the pressure discontinuity between elements, we apply integration by parts twice on the second term following Salinas et al. [43] and Al Kubaisy et al. [4], which yields

$$\sum_{\Omega_e \in \Omega} \left[\int_{\Omega_e} \mathbf{\Phi_i} \cdot \mathbf{v}_t \, d\Omega_e + \int_{\Omega_e} \left(\mathbf{\Phi_i} \cdot \lambda_t \mathbf{K} \right) \cdot \nabla p \, d\Omega_e - \int_{\Gamma_e} \left(\mathbf{\Phi_i} \cdot \lambda_t \mathbf{K} \tilde{p} \right) \cdot \mathbf{n} \, d\Gamma_e + \int_{\Gamma_e} \left(\mathbf{\Phi_i} \cdot \lambda_t \mathbf{K} p \right) \cdot \mathbf{n} \, d\Gamma_e \right] = 0, \tag{10}$$

where Γ_e is the element boundary, $\mathbf{n}$ is the unit normal vector and $\tilde{p}$ corresponds to the pressure of the neighboring element that shares an interface with element Ω_e. We combine the third and fourth terms on the left hand side into a single term that is referred to here as the jump term (see also [4]). The finite element approximations, shown in Eqn. (7) and (8), for the velocity and pressure, respectively, are substituted in Eqn. (10), which gives

$$\sum_{\Omega_e \in \Omega} \sum_{j=1}^{N_v} \int_{\Omega_e} \mathbf{\Phi_i} \cdot \mathbf{\Phi_j} v_{t,j} \, d\Omega_e + \sum_{\Omega_e \in \Omega} \sum_{k=1}^{N_p} \int_{\Omega_e} \left(\mathbf{\Phi_i} \cdot \lambda_t \mathbf{K} \right) \cdot \nabla \Psi_k p_k \, d\Omega_e + \sum_{\Gamma_e \in \Omega} \sum_{k=1}^{N_p} \oint_{\Gamma_e} \left(\mathbf{\Phi_i} \cdot \lambda_t \mathbf{K}_h \Psi_k \left(p_k - \tilde{p}_k \right) \right) \cdot \mathbf{n} \, d\Gamma_e = 0, \tag{11}$$

N_v is the total count of velocity nodes, N_p is the total count of pressure nodes, and $\mathbf{K}_h$ denotes the harmonic mean permeability of the two neighboring elements that share the interface (Γ_e). The jump term described here differs from the one defined in the HyCVFE method [4]; by construction of the SM-CVFE method, the jump term contribution is nonzero between all neighboring

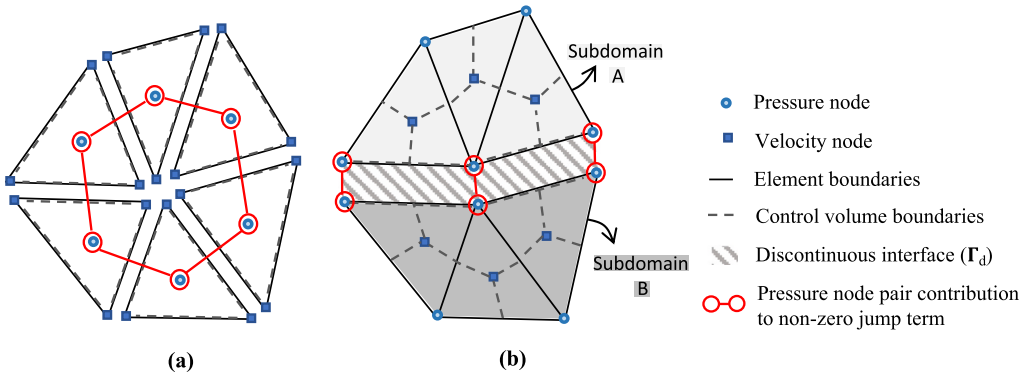

Fig. 3. Snippet of a mesh comparison for the discretization of **(a)** the SM-CVFE method and **(b)** the HyCVFE method [4] with 2 subdomains. The SM-CVFE discretization applies the jump term for all neighboring elements while the HyCVFE method incorporates the jump term solely along subdomain boundaries.

elements (Fig. 3a), whereas the HyCVFE method incorporates a nonzero jump term only for elements at subdomain boundaries (Γ_d) (Fig. 3b).

In the SM-CVFE approach, since the pressure is represented element-wise, the second term in Eqn. (11) vanishes because the derivative of the pressure basis function is zero. This approach for derivation of the new element pair ($P_{1,DG} - P_{0,DG}$) achieves the final discretized form of Darcy's equation as

$$\sum_{\Omega_e \in \Omega} \sum_{j=1}^{N_v} \int_{\Omega_e} \mathbf{\Phi_i} \cdot \mathbf{\Phi_j} v_{t,j} \, d\Omega_e + \sum_{\Gamma_e \in \Omega} \sum_{k=1}^{N_p} \oint_{\Gamma_e} \underbrace{\left(\mathbf{\Phi_i} \cdot \lambda_t \mathbf{K}_h \Psi_k \left(p_k - \tilde{p}_k \right) \right) \cdot \mathbf{n}}_{\text{jump term}} \, d\Gamma_e = 0. \tag{12}$$

Contrary to the presented method, the HyCVFE applies a first order approximation for pressure, and thus the derivative of the pressure basis function does not vanish; the term analogous to the second term on the left hand side of Eqn. (11) is non-zero for the HyCVFE method.

3.3. Discretization of the continuity equation

In our SM-CVFE approach, the control volume mesh is the same as the element mesh. Consider Ω_e that denotes the element entity at which flux continuity is applied. In order to derive the weak form of the continuity equation, Eqn. (3), we multiply with Ψ_i, the pressure basis function, and integrate over the computational domain (Ω). We then substitute the finite element velocity approximation, Eqn (7) as follows

$$\sum_{\Omega_e \in \Omega} \sum_{j=1}^{N_v} \int_{\Omega_e} \Psi_i \nabla \cdot \mathbf{\Phi_j} v_{t,j} \, d\Omega_e - \sum_{\Omega_e \in \Omega} \int_{\Omega_e} \Psi_i q_t \, d\Omega_e = 0. \tag{13}$$

Next, we use the divergence theorem for transforming the volume integral of the first term which yields

$$\sum_{\Gamma_e \in \Omega} \sum_{j=1}^{N_v} \int_{\Gamma_e} \Psi_i \left(\mathbf{\Phi_j} \tilde{v}_{t,j} \right) \cdot \mathbf{n} \, d\Gamma_e - \sum_{\Omega_e \in \Omega} \int_{\Omega_e} \Psi_i q_t \, d\Omega_e = 0, \tag{14}$$

with $\tilde{v}_t$ indicating the velocity approximation over the control volume boundary (Γ_{cv}). We describe how to compute $\tilde{v}_t$ in section 3.6. The first term in Eqn. (14) accounts for fluxes between elements while the second term incorporates source terms.

3.4. Discretization of the transport equation

Consider the mass conservation equation, Eqn. (5) where we apply the spatial discretization over the elements (Ω_e) and an explicit time discretization. Since the fractional flow term is a function of saturation that can be nonlinear (a quadratic or even a cubic function), we linearize the term (f_α) in the saturation equation, see Eqn. (2) and (4). Finally, to determine the saturation of phase α (S_α), we use the integral-form of the equation, given by

$$\int_{\Omega_e} \frac{\phi (S_{\alpha,e}^{n+1} - S_{\alpha,e}^{n})}{\Delta t} d\Omega_e = - \oint_{\Gamma_e} \left(f_{\alpha,e}^{n} \tilde{\mathbf{v}}_t^{n+1} + \frac{\partial f_{\alpha,e}}{\partial S_{\alpha,e}} \bigg|^{n} (S_{\alpha,e}^{n+1} - S_{\alpha,e}^{n}) \tilde{\mathbf{v}}_t^{n+1} \right) \cdot \mathbf{n} d\Gamma_e + \int_{\Omega_e} q_\alpha d\Omega_e, \tag{15}$$

with the superscripts n and Δt denoting the time step and the time step size, respectively.

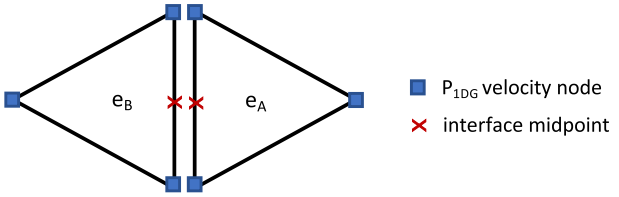

Fig. 4. Diagram of two neighboring elements e_A and e_B to demonstrate the velocity approximation along an interface.

3.5. Coupled flow and transport

In the implementation of the coupled flow and transport of the SM-CVFE method presented here, we use an implicit-pressure explicit-saturation (IMPES) based approach. This solution approach is commonly used as it is straightforward to implement for validation and testing [4]. For completeness, the IMPES coupling approach is briefly described as follows. The stability of the system is achieved by restricting the Courant–Friedrichs–Lewy (CFL) number such that CFL < 1 [5]. The range of CFL numbers tested in this study spans from 0.01 to 0.1. For the flow model, we combine Eqn. (12) and (14) to construct the algebraic system given by

$$\begin{cases} \mathbf{A}\mathbf{v}_t^{n+1} + \mathbf{B}p^{n+1} & = b_1 \\ \mathbf{C}\mathbf{v}_t^{n+1} & = b_2 \end{cases} \tag{16}$$

where **A** denotes the mass matrix, and **B** is the stiffness matrix that is assembled by the jump term connecting neighboring elements; see the first and second terms, respectively, in Eqn. (12). **C** is the divergence-free operator computed by the first term in Eqn. (14). The IMPES-based approach involves solving the flow model while assuming the saturation field is unchanged. The primary flow unknowns, $\mathbf{v}_t^{n+1}$ and p^{n+1}, described in Eqn. (16), can be solved simultaneously or by using a projection-based approach [15,46]. We employ the latter approach where the pressure is first resolved by eliminating the velocity unknown. Then the velocity is determined by substituting the pressure solution in Eqn. (12). Next, the saturation is solved explicitly via Eqn. (15).

3.6. Interface approximations

The velocity approximation at the interfaces between elements and, therefore, control volumes of the SM-CVFE is constructed by evaluating the effective contribution of the element velocity at the midpoint on either side of the interface, denoted by $\mathbf{v}_{t,e_A}$ and $\mathbf{v}_{t,e_B}$. These are combined using a permeability-weighted harmonic average as described in Al Kubaisy et al. [4]:

$$\tilde{\mathbf{v}}_t(\mathbf{x}) = \frac{1}{2}\left(\mathbf{K}_h\mathbf{K}_{e_A}^{-1}\mathbf{v}_{t,e_A}(\mathbf{x}) + \mathbf{K}_h\mathbf{K}_{e_B}^{-1}\mathbf{v}_{t,e_B}(\mathbf{x})\right), \tag{17}$$

where $\tilde{\mathbf{v}}_t$ is the velocity approximation on the interface shared by the two elements e_A and e_B, $\mathbf{K}^{-1}$ is the inverse of the element permeability, and $\mathbf{x}$ is the midpoint position on the interface. The schematic of two neighboring elements is shown in Fig. 4. By construction of the SM-CVFE approach, the velocity in each element is not uniform and differs based on the location of the midpoint, due to the first order Lagrangian approximation used for velocity. Therefore, the velocity on each interface of an element is not the same. The described velocity approximation is applied in the coefficients of the divergence-free operator (**C**), Eqn. (14), and in the saturation equation, Eqn. (15). We adopted a first-order upwind scheme to approximate saturation dependent properties at the interface, including the total mobility, the fractional flow term, and the derivative of the fractional flow term. In the next section, we show that the scheme is effective in producing stable, mass conservative, and monotonic solutions.

4. Numerical experiments

The validation of the SM-CVFE approach for the single phase model and two phase flow model are shown in experiments 4.1 and 4.2. We share the convergence with respect to the semi-analytical Buckley-Leverett solution [11]. Then we demonstrate the performance of the SM-CVFE in three additional experiments with geometrical complexities. In experiment 4.3 we test two fracture-barrier intersection scenarios. Next, geostatistical fields are generated for a single channel with meandering geometry and a challenging flow system of intersecting channels in experiments 4.4 and 4.5, respectively.

The relative permeability for two phase flow that we incorporated in our implementation is the Brooks-Corey model [10] given by

$$k_{rw}(S_w) = \left(\frac{S_w - S_{w,r}}{1 - S_{w,r} - S_{nw,r}}\right)^{n_w}, \tag{18}$$

and

$$k_{rnw}(S_w) = \left(\frac{1 - S_w - S_{nw,r}}{1 - S_{w,r} - S_{nw,r}}\right)^{n_{nw}}, \tag{19}$$

Table 1
Model setup for the numerical experiments.

	Numerical experiment				
	4.1	4.2	4.3	4.4	4.5
X-axis domain length (L_x)	1.	1.	1.	1.	1.
Y-axis domain length (L_y)	0.05	0.05	1.	0.5	1.
Porosity (ϕ)	0.1	0.1	variable	0.1	0.1
Corey exponent of wetting phase (n_w)	N/A	2.	1.	2.	2.
Corey exponent of non-wetting phase (n_{nw})	N/A	2.	1.	2.	2.
Residual wetting saturation ($S_{w,r}$)	N/A	0.2	0.	0.2	0.2
Residual non-wetting saturation ($S_{nw,r}$)	N/A	0.3	0.	0.3	0.3
Viscosity ratio (μ_{nw}/μ_n)	N/A	2.	2.	2.	2.

Table 2
Comparison of the DoF requirements in the numerical experiments.

Numerical experiment	Number of elements	CVFE DoF	SM-CVFE DoF	Factor (increase)
4.1 (case I and II, $n_x = 40$)	160	443	1120	2.53
4.1 (case I and II, $n_x = 80$)	320	883	2240	2.53
4.1 (case I and II, $n_x = 160$)	640	1763	4480	2.54
4.2 ($n_x = 40$)	160	566	1280	2.26
4.2 ($n_x = 80$)	320	1126	2560	2.27
4.2 ($n_x = 160$)	640	2246	5120	2.28
4.3 (case I)	1280	3934	10240	2.60
4.3 (case II)	1310	4024	10480	2.60
4.4 (case I, uniform mesh)	591	1844	4728	2.56
4.4 (case II, uniform mesh)	1428	4394	11424	2.60
4.4 (case III, uniform mesh)	2992	9132	23936	2.62
4.4 (non-uniform mesh)	3583	10834	N/A	N/A
4.5	3900	N/A	31200	N/A

where $S_{\alpha,r}$ and n_α are the residual α phase saturation and the Corey exponent of α phase, respectively. The parameters of the numerical experiments are provided in Table 1.

The computational efficiency of the numerical experiments is compared using the Degrees of Freedom (DoF) or the total number of unknowns in a given time step. We use

$$DoF = N_p + N_v + N_s, \tag{20}$$

to describe the computational requirements of the approximation where N_s denotes the saturation DoF, equivalent to the total count of control volumes. In Table 2, we highlight the DoF requirements used in the following numerical experiments.

4.1. Single phase flow

The validation for single phase flow is captured in two pseudo one-dimensional cases. In case I, a homogeneous medium is used with pressure boundary conditions applied on the left and right, with the top and the bottom boundaries set to no-flow. Case II has a similar setup except that the permeability is heterogeneous. The mesh used in the model is shown in Fig. 5a where the number of elements along the x-axis (n_x) is 40, while the permeability of cases I and II are shown in Fig. 5b and 5c, respectively. The steady state solution of pressure (Fig. 5d) is a straight line for case I while the heterogeneity introduced in case II is reflected in the solution as a change of slope at position $x = 0.5$. In case II, the right region, shown between $[0.5, 1.0]$, has half the slope of the left region, between $[0., 0.5]$ which is correct with the change of property. The continuous pressure solution obtained using the classical CVFE method on the same mesh is shown in Fig. 5d and corroborates the SM-CVFE results. In both cases, the DoF_{CVFE} and $DoF_{SM-CVFE}$ are 443 and 1,120, respectively, see Table 2. Thus, the SM-CVFE method requires 2.5 times more degrees of freedom than the CVFE method, similar requirements to the MFE method [19,22]. The increase of the SM-CVFE method computational requirements is attributed to a higher resolution of the control volume mesh that is consistent with the element mesh and one higher order of the velocity approximation compared to the CVFE method. To demonstrate the convergence of the SM-CVFE approach, we refine the mesh along the x-axis (n_x = 80 and 160). In both cases, the proposed SM-CVFE method yields linear convergence, see Fig. 5e.

4.2. Buckley-Leverett problem

For the two phase model validation, we simulate the Buckley-Leverett problem on a pseudo one-dimensional, homogeneous domain. The domain is discretized with several mesh resolutions in the direction of the x-axis ($n_x = 40, 80, 160$). The model setup is

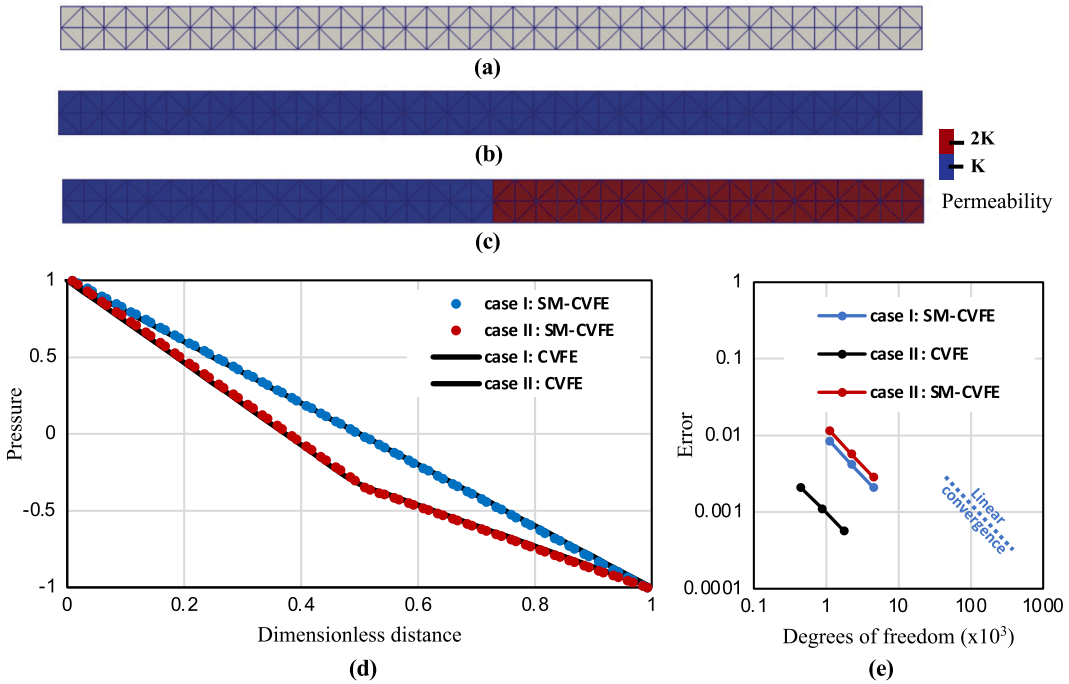

Fig. 5. The single phase validation model experiment 4.1: **(a)** The mesh discretized with 40 elements along the x-axis. **(b)** Case I permeability field. **(c)** Case II permeability field. **(d)** Comparison of pressure solution of both cases, I and II. **(e)** Convergence of the pressure solutions for both cases. For case I, the CVFE pressure solution is found in perfect agreement with the exact, analytical solution (not included in the plot).

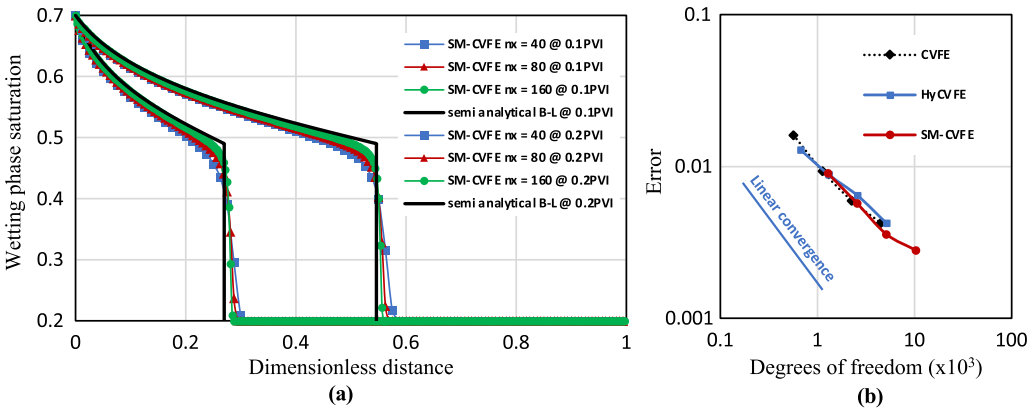

Fig. 6. The two phase validation model in experiment 4.2 for the Buckley-Leverett problem. **(a)** The convergence of numerical SM-CVFE method to the semi-analytical solution as the mesh is refined. The two clusters of curves refer to 0.1 and 0.2 PVI. For the numerical comparison, we use several mesh resolutions along the x-axis including 40, 80, and 160 elements. **(b)** A comparison of the L^1 norm of the error for the reference CVFE method, the HyCVFE method and the developed SM-CVFE method.

as follows: the initial non-wetting phase saturation ($S_{nw,i}$) is 0.8, and the residual wetting phase saturation (S_{wr}) is 0.2. We inject the wetting phase from the left to the right whereas the top and bottom have no-flow boundary conditions. Fig. 6a provides a comparison of the SM-CVFE saturation solution to the semi-analytical Buckley-Leverett reference solution after 0.1 and 0.2 pore volume injected (PVI). We observe that the agreement between the numerical and semi-analytical solution is improved as the mesh is refined. We demonstrate that the system is locally and globally mass conservative from the representative area under the cluster of curves; for each time step, the area under the curve represents the same wetting phase mass injected into the system. Fig. 6b compares the L1 norm of the saturation solution error of the SM-CVFE method and the classical CVFE with respect to the semi-analytical solution. The overlap of the two curves indicates that for a given number of degree of freedom, the error is essentially the same in both methods. Additionally, both curves follow the same convergence trend as we increase the mesh resolution and provide near linear convergence.

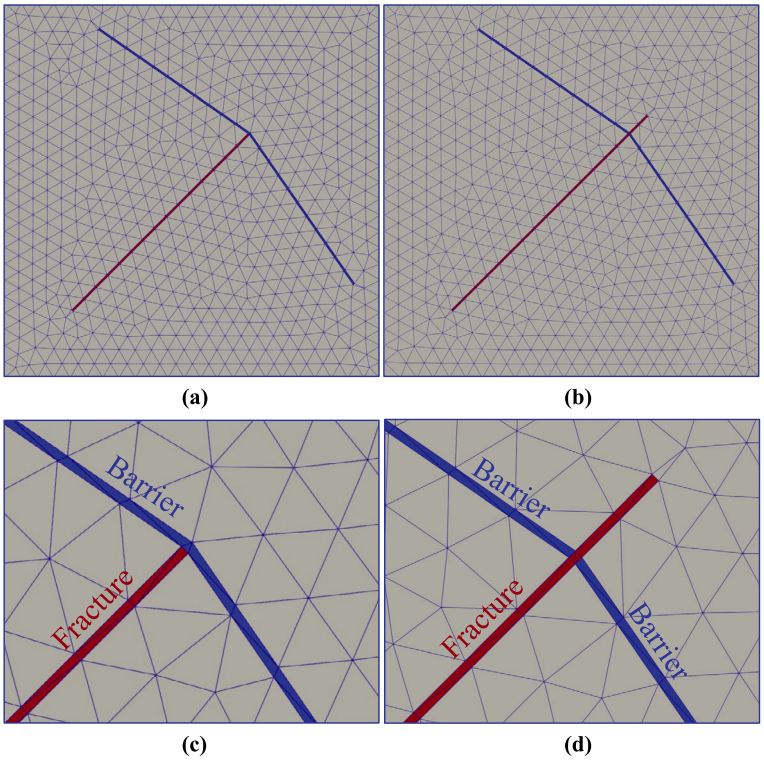

Fig. 7. The mesh for experiment 4.3. The background, the fracture, and the barrier regions are denoted by gray, red, and blue colors, respectively. Case I: the fracture reaching the barrier without crossing through shown in **(a)** and the close up in **(c)**. Case II: the fracture penetrating the barrier in **(b)** and the close up in **(d)**. (For interpretation of the colors in the figure(s), the reader is referred to the web version of this article.)

Table 3
Geometry and petrophysical properties of different regions for experiment 4.3.

	Fracture	Barrier	Background
Aperture	$0.005656L_x$	$0.005656L_x$	N/A
Porosity	1.	0.	0.1
Log permeability	6.	-6.	0.

L_x denotes the length of the domain with respect to the x-axis.

4.3. Fracture-barrier intersection

The experiment described here is adopted from Hoteit and Firoozabadi [27]. We explore both of their cases I and II. In case I, a highly permeable fracture spans diagonally from the bottom left to the top right of the domain such that it reaches a barrier without crossing it (Fig. 7a and close up in Fig. 7c). Case II is similar except that the fracture penetrates the barrier (Fig. 7b and close up in Fig. 7d). Fracture and barrier petrophysical properties are provided in Table 3. We apply pressure boundary conditions from the bottom left corner to the top right corner and the wetting phase is injected at the bottom left corner. The remaining domain boundaries are set to no-flow. The number of elements in cases I and II are 1,280 and 1,310, respectively.

We compare the saturation solutions obtained using the proposed SM-CVFE and the classical CVFE method for both cases (Fig. 8). For the early time step (Fig. 8a-b and Fig. 8e-f for case I and II, respectively), the saturation front of the proposed SM-CVFE method reaches the barrier whereas the CVFE solutions exhibit overall delay in the saturation fronts. At the later time step, we observe in both cases the injected fluid phase migration beyond the barrier in Fig. 8 c-d and Fig. 8 g-h with different flow behaviors in the fracture and barrier regions which in turn affect the flow in the matrix region. In both cases, the solutions of the classical CVFE method emphasize the inconsistency to preserve material properties due to the two mesh approach in comparison to the single mesh approach. The DoF_{CVFE} and $DoF_{SM-CVFE}$ for case I are 3,934 and 10,240, respectively, while case II required 4,024 and 10,480, respectively, see Table 2.

Next, we compare the saturation solutions of the classical CVFE, the proposed SM-CVFE, and the MFE-DG method [27] in Fig. 9. It is worth mentioning the differences in the approach and the employed mesh; the MFE-DG approach represented the fractures and barriers as lower dimensional entities and employed a mesh that is slightly different to the one used in the CVFE and the SM-CVFE results. Moreover, the MFE-DG method applied a slope limiter in the formulation to reduce the numerical dispersion of the saturation solution. Despite the aforementioned differences, after 0.5 PVI the flow patterns around the fracture and barrier in both cases I and

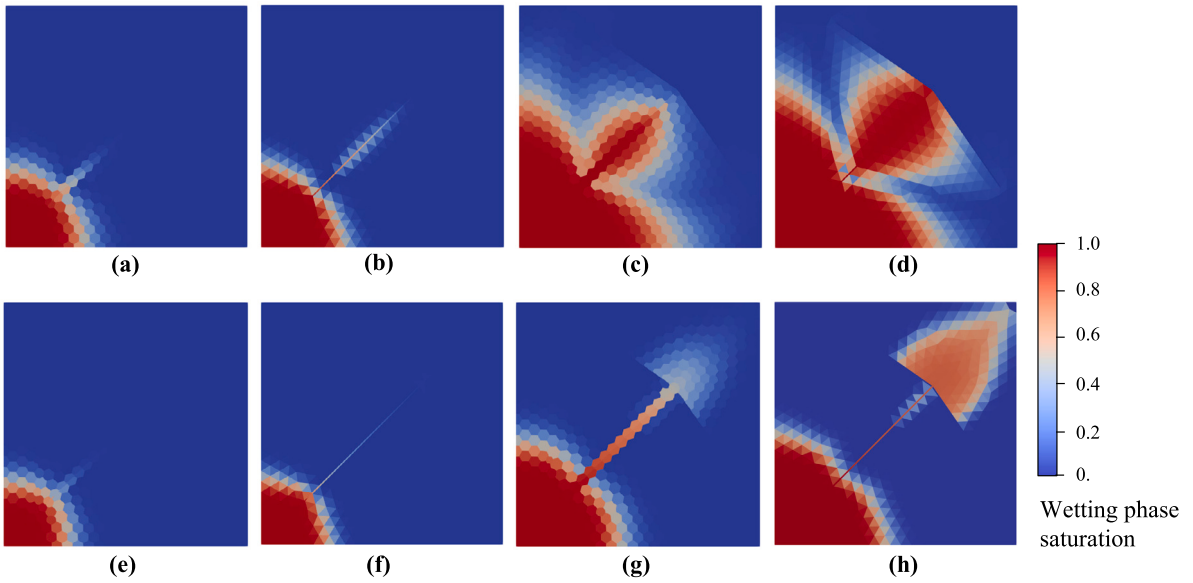

Fig. 8. The wetting phase saturation solution for experiment 4.3. The top row refers to case I. The solution after 0.08 PVI is shown in **(a)** and **(b)** for the CVFE method and the SM-CVFE method, respectively. After 0.5 PVI, the solution is shown in **(c)** and **(d)** for the CVFE method and the SM-CVFE method, respectively. The bottom row features case II. After 0.05 PVI, the solution is shown in **(e)** and **(f)** for the CVFE method and the SM-CVFE method, respectively. After 0.5 PVI the solution is shown in **(g)** and **(h)** for the CVFE method and the SM-CVFE method, respectively.

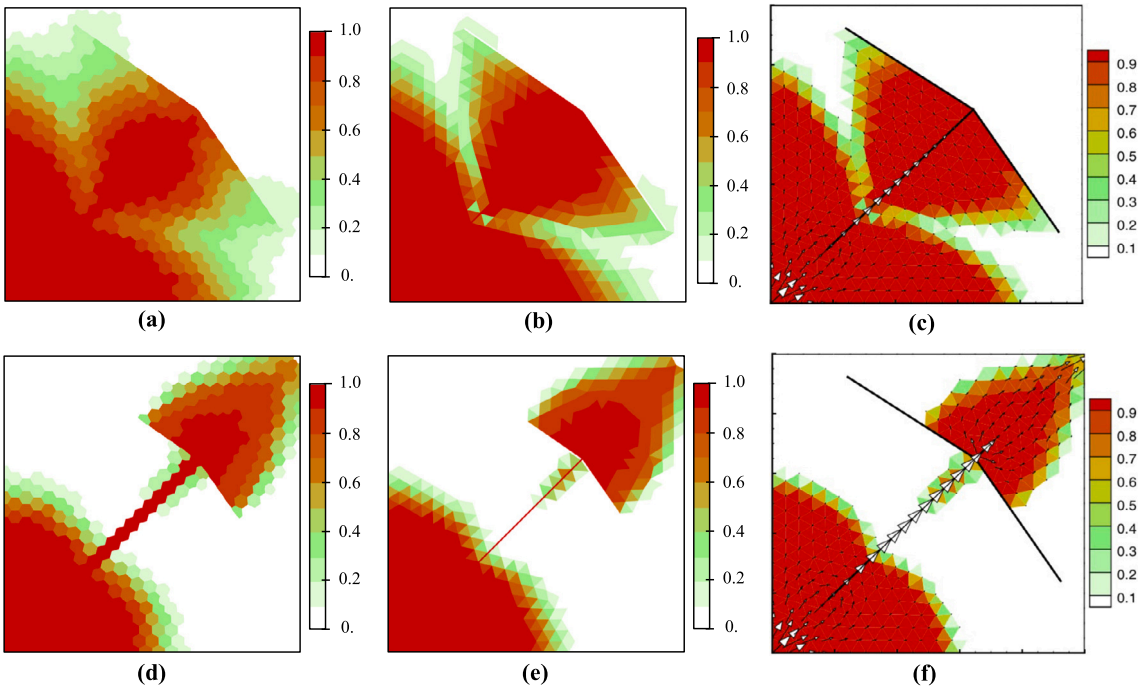

Fig. 9. The saturation solution comparison including the results of MFE-DG method from Hoteit and Firoozabadi [27] for experiment 4.3 at 0.5 PVI. For comparison purposes, the color map used here follows the one used by Hoteit and Firoozabadi [27]. The top row shows case I results using the classical CVFE in **(a)**, the SM-CVFE in **(b)**, and the MFE-DG by Hoteit and Firoozabadi [27] in **(c)**. The bottom row shows case II using the classical CVFE in **(d)**, the SM-CVFE in **(e)**, and the MFE-DG by Hoteit and Firoozabadi [27] in **(f)**. The results shown in **(c)** and **(f)** were obtained from Fig. 12 in [27].

II for the SM-CVFE and the MFE-DG are remarkably similar and are different to the solution obtained using the CVFE method. The reason is essentially due to the use of a single mesh approach that is analogous to the MFE. The SM-CVFE solutions presented in this experiment are comparable to those obtained using specialized numerical methods that include, but are not limited to, discrete fracture networks (DFN) within the mixed finite element frameworks.

Table 4
The parameters used to generate the spatial permeability fields (GSTools package) for experiment 4.4.

Region	Channel	Background
Variogram	exponential	exponential
Dimensions	2	2
Length scale	1.	0.4
Anisotropy ratio	1.	0.3
Seed	200000	100000
Nugget	0.	0.
Variance	1.	1.
increment*	6	0

* Parameter used as a post-processing step to combine the fields.

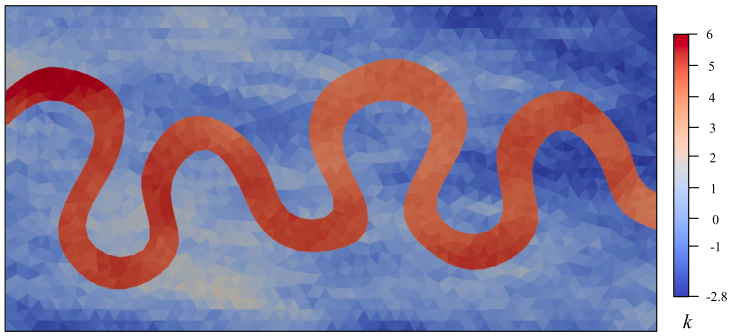

Fig. 10. The log permeability distribution of experiment 4.4. The channel region is denoted with high permeability values. This permeability distribution refers to case III with 2992 elements.

4.4. Meandering channel flow

The aim of the experiment is to highlight the effectiveness of the SM-CVFE formulation to capture accurate solutions of models with element to element variability in the underlying petrophysical properties while simultaneously eliminating the undesirable artificial mass leakage effects exhibited by the control volumes spanning different permeability regions in the classical CVFE method. We consider a channelized sand-shale system comprised of a high permeability channelized sand body embedded in a low permeability, shale background. The permeability distribution is shown in Fig. 10 where two fields were generated then combined to create a bimodal permeability distribution. A geostatistical tool was used to generate those fields; GSTools python package used with the parameters provided in Table 4. We use several mesh resolutions in this model with the total elements of 591, 1428, and 2992 for cases I, II, and III, respectively. The average variance of the permeability distribution is preserved for all cases. The pressure boundary conditions are applied from the left to the right of the domain while the wetting phase is injected from the left boundary. The top and the bottom boundaries are set to no-flow.

We compare the saturation solution obtained using the classical CVFE method for cases I-III (see Fig. 11a-c) after 0.03 PVI. In case I, the left winding of the meander produces a non-physical connection in the channel, see Fig. 11a, as a result of the construction of the coarse control volume dual mesh. Case II uses relatively smaller control volumes which prevent the non-physical connection; however, the leakage exhibited around the channel is still considerable. Finally, case III utilizes the finest tested mesh which reduces the leakage around the channel. From Fig. 11a-c we note that, at a given time step, the location of the wetting phase front differs considerably as the mesh is refined while using the CVFE method because a coarse mesh contributes to additional loses of injected fluid smeared across the large sand-shale interface, delaying the propagation of the saturation front in the channel region. Second, the meandering of the channel exaggerates the effect of the leakage when compared to a straight channel path. The meandering of the channel creates a larger interface with the background region and, therefore, increases the leakage effects. The CVFE method is inadequate to capture the flow and transport dynamics without exploiting a very fine mesh. Now consider the saturation solutions provided in Fig. 11d-f which show the corresponding SM-CVFE solution for cases I-III, respectively. We observe excellent agreement of the saturation front for the SM-CVFE solution at a given time step irrespective of the mesh size, due to the use of single mesh that eliminates the non-physical mass leakage in the transport solution. We note that the effect of numerical dispersion of the saturation front is reduced as we refine the mesh (Fig. 11d compared to Fig. 11e and Fig. 11f) that is consistent with convergence analysis demonstrated in numerical experiment 4.2.

We quantify each method's mesh sensitivity with respect to the non-physical leakage. We compute the non-physical leakage to in the low permeability, background region (Ω_{low}) using:

$$\epsilon_{max} = \frac{\sum_{k\in\Omega_{low}} \left(S_{w,k} - S_{w,r,k}\right)\Omega_{cv,k}}{\sum_{k\in\Omega_{low}} \Omega_{cv,k}} \tag{21}$$

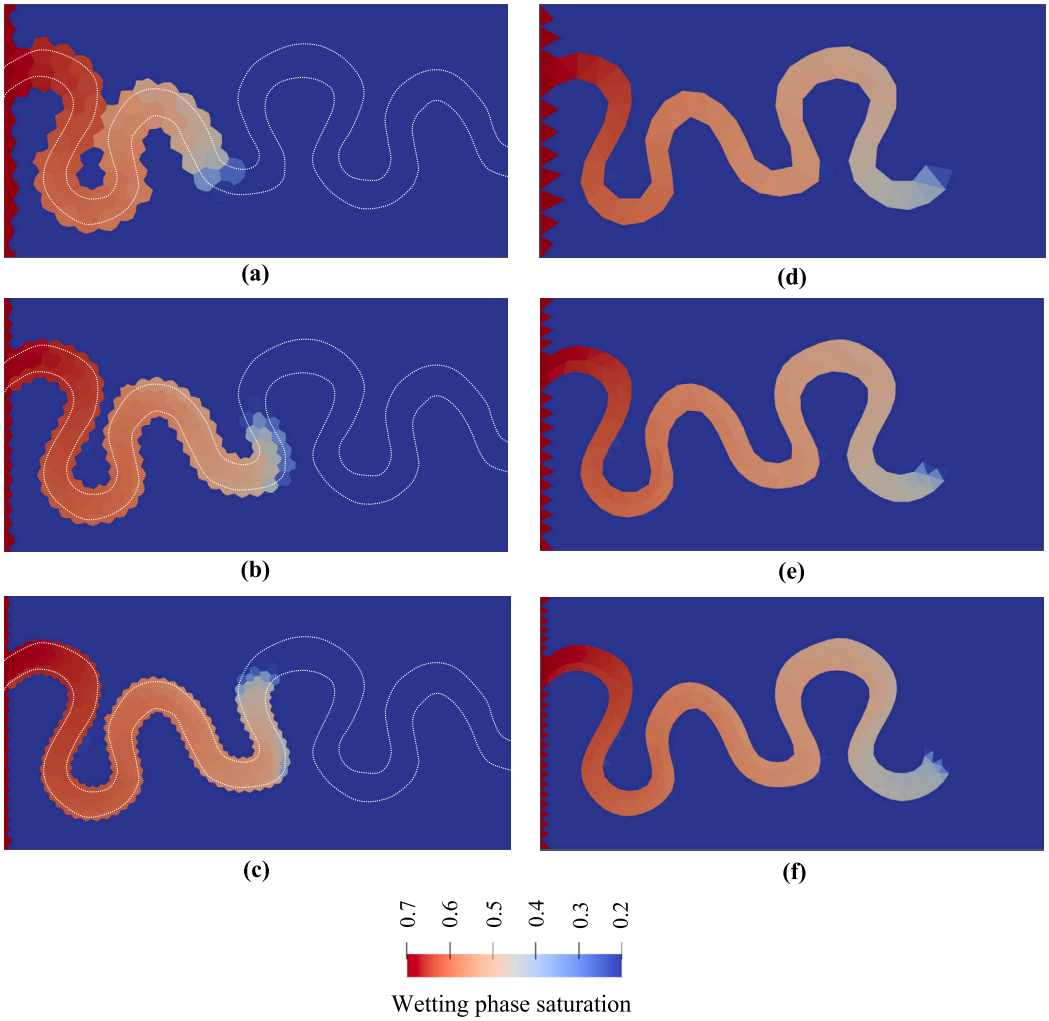

Fig. 11. The wetting phase saturation of experiment 4.4 after 0.03 PVI. The saturation distribution of the classical CVFE method solution is displayed on the left column and the SM-CVFE method is displayed to the right. Case I: the coarse mesh in **(a)** and **(d)**. Case II: medium refinement in **(b)** and **(e)**. Case III: the fine mesh in **(c)** and **(f)**. Note that the left boundary's inlet saturation that does not coincide with the channel is not accounted for in the PVI approximation in order to eliminate the irrelevant mesh effects from our study. We include an outline of the channel boundaries on the left column to emphasize the leakage along the boundaries as we refine the mesh in cases I, II, and III.

where $S_{w,k}$ is the wetting phase saturation of control volume k, $S_{w,r,k}$ is the residual wetting saturation of control volume k, and $\Omega_{cv,k}$ is the control volume. This approach follows the work of Salinas et al. [43] and Al Kubaisy et al. [4] in order to quantify the undesirable leakage effects in the saturation solution. Fig. 13a compares the non-physical leakage (ϵ_{max}) in the SM-CVFE and the CVFE methods. We observe a consistent improvement in the saturation solution of the SM-CVFE such that the leakage is reduced by more than 2 orders of magnitude compared to the CVFE approach. Additional refinement of the mesh in the CVFE does not close the 2 order of magnitude gap with the SM-CVFE.

Next, we extend this experiment with an additional case for the reference CVFE method to accommodate non-uniform meshes. As shown in Fig. 12a, the mesh refinement is applied near the interface between the channel and background region. The saturation solution in Fig. 12b, captured after 0.03 PVI, shows the saturation front has advanced further into the channel compared to previous cases (I-III). However, we note that the position accuracy of this saturation front is not comparable with that achieved by the SM-CVFE method. This case highlights the necessity of minimizing control volumes that span different regions when employing the CVFE method. Ideally, the control volume size need to approach zero to yield solutions comparable to those obtained with the SM-CVFE approach.

The blue cross shown in Fig. 13a refers to the non-uniform mesh employed for the CVFE method. Despite the marginal improvement in leakage reduction, a comparison for equivalent DoF between the SM-CVFE (uniform mesh) and CVFE (non-uniform mesh) methods reveals that the SM-CVFE method still exhibits a two order of magnitude improvement in accuracy compared to the classical CVFE method.

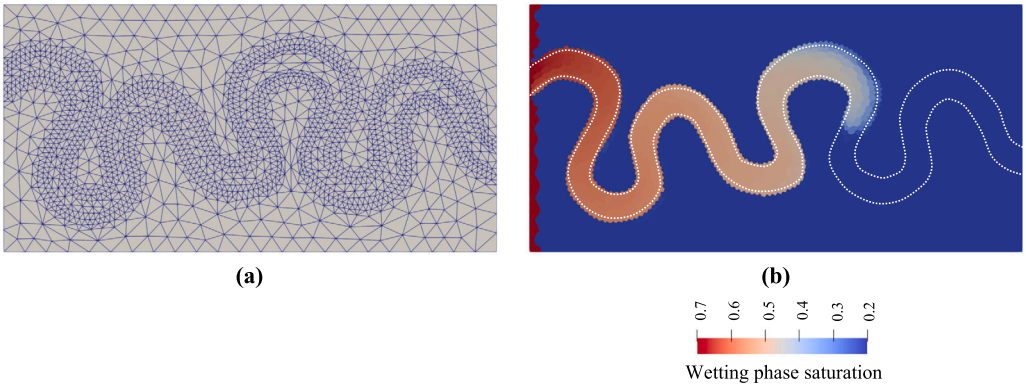

Fig. 12. (a) The non-uniform mesh for experiment 4.4. Refinement is applied near the channel boundaries. **(b)** The wetting phase saturation of the CVFE method after 0.03 PVI.

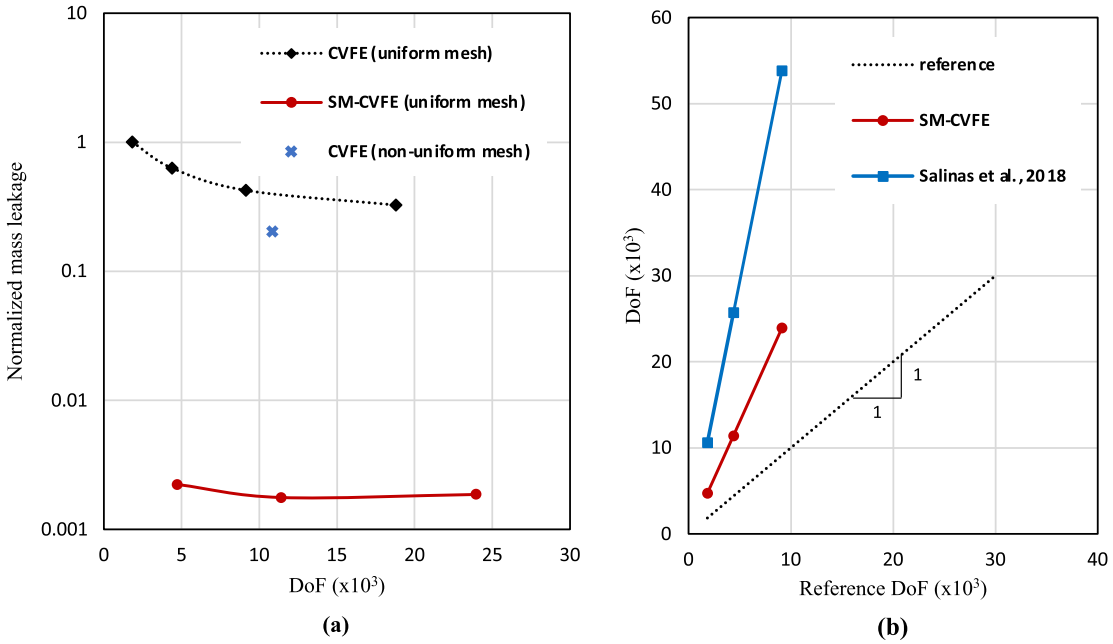

Fig. 13. Comparison of different methods in experiment 4.4. **(a)** The mass leakage plot for the reference CVFE method and the proposed SM-CVFE method as we refine the mesh. We observe about two orders of magnitude improvement in the solution of the SM-CVFE compared to the reference solutions for both uniform and non-uniform meshes.**(b)** Comparison of the DoF requirements as the mesh is refined showing the reference CVFE, the proposed (SM-CVFE) method, and Salinas et al. [43] method. The dotted line has a slope of one and is used as a reference to the CVFE method's computational requirements.

Finally, we compare the DoF of the reference CVFE with the SM-CVFE and the Salinas et al. [43] approximations in Fig. 13b. The cross-plot enables us to compare the computational requirements of the different methods for a given mesh. The CVFE reference unit slope is a benchmark. The SM-CVFE method computational requirements are slightly less than half that of the Salinas et al. [43] method despite both approximations relying on discontinuous discretization techniques. The SM-CVFE is more effective since it is based on a lower order approximation while employing a single, consistent mesh; it requires about 2.5 times the DoF of the reference CVFE method for the same mesh. In this experiment we show that the saturation solution obtained from the SM-CVFE exhibits significant reduction in the undesirable leakage compared to the reference CVFE independent of the mesh resolution. When modeling flow through complex geometry, this approximation outperforms conventional methods due to the elimination of the secondary mesh that introduces inaccurate solutions along subdomain interfaces. In the SM-CVFE method, the ability to capture accurate flow model in complex geometrical domains stems from the use of unstructured, flexible elements rather than mesh refinement.

4.5. Intersecting channels

In this experiment, we introduce a complex 2D domain of intersecting channels with the permeability distribution shown in Fig. 14. Similar to the previous experiment, we generate several geostatistical fields then combine them to create the final permeability distribution. We note that the high permeability regions are concentrated in the channels (1-5 in Fig. 14) where it is nonuniform

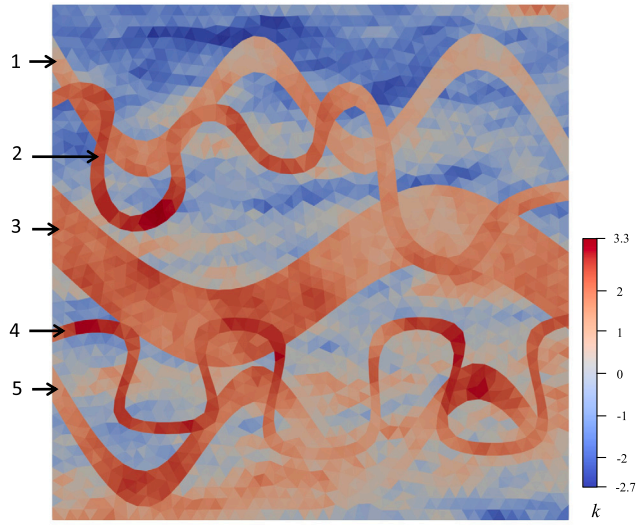

Fig. 14. The log permeability distribution of experiment 4.5. The numbers to the left aid to identify individual channels in the text.

Table 5
The parameters used to generate the spatial permeability fields (GSTools package) for experiment 4.5.

Region	Irregular channel	Sinusoidal channel	Background
Variogram	exponential	exponential	exponential
Dimensions	2	2	2
Length scale	1.	1.	0.4
Anisotropy ratio	1.	1.	0.3
Seed	208	208	62534
Nugget	0.	0.	0.
Variance	1.	1.	1.
increment*	1.5	1.	0

* Parameter used as a post-processing step to combine the fields.

and spans a wide range of values. The setup parameters needed to generate the geostatistical permeability fields are provided in Table 5. In the table, the irregular channel settings are used for channels 2 and 4, while the sinusoidal channel refers to channels 1, 3, and 5. A single mesh resolution is demonstrated in this experiment where the domain is discretized into 3,900 triangular elements and the corresponding $DoF_{SM-CVFE}$ required for modeling the coupled flow and transport is 31,200 (Table 2). Pressure boundary conditions are applied from the left to the right boundary while injection of the non-wetting phase is taking place from the left boundary. The top and bottom boundaries are set to no-flow.

We provide the saturation solution at several time steps in Fig. 15. After 0.03 PVI (Fig. 15a) the saturation solution shows the migration of injected fluid phase from channels 4 to 3, as well as the inter-connectivity between channels 1 and 2 as a result of intersections near the inlet. The next time step shown in Fig. 15b refers to the saturation solution after 0.07 PVI with the injected fluid advanced over half way through channel 3 which provides the shortest flow path to the outlet. After breakthrough, both Fig. 15c and 15d show that the overall sweep through the bottom region is more efficient when compared to the top region. In this example, we demonstrate that the general SM-CVFE approach is applicable to model flow and transport through complex intersecting domains, including highly heterogeneous and nonuniform permeability fields.

5. Discussion

In this paper, we have described the original formulation of the single-mesh CVFE (SM-CVFE) method and demonstrated the versatility of the approach using several numerical experiments featuring domains with complex geometries. In the last two numerical experiments, 4.4 and 4.5, we constructed highly heterogeneous, geostatistical permeability fields. Those are challenging to resolve accurately without resorting to a very fine mesh when using the classical CVFE approach especially along boundaries between subdomains. Now consider a slight modification to the last two experiments where we assign distinct permeability values and apply them uniformly to each region [42,31]. The use of HyCVFE method [4] will outperform the proposed SM-CVFE, the MFE, the classical CVFE, and the Salinas et al. [43] methods. In such a model, the uniform permeability regions are accurately and efficiently resolved using the subdomain approach where we combine the continuous pressure approximation in homogeneous subdomains while exclusively assigning hybrid nodes that account for jumps in the solution along material boundaries, by preventing the control

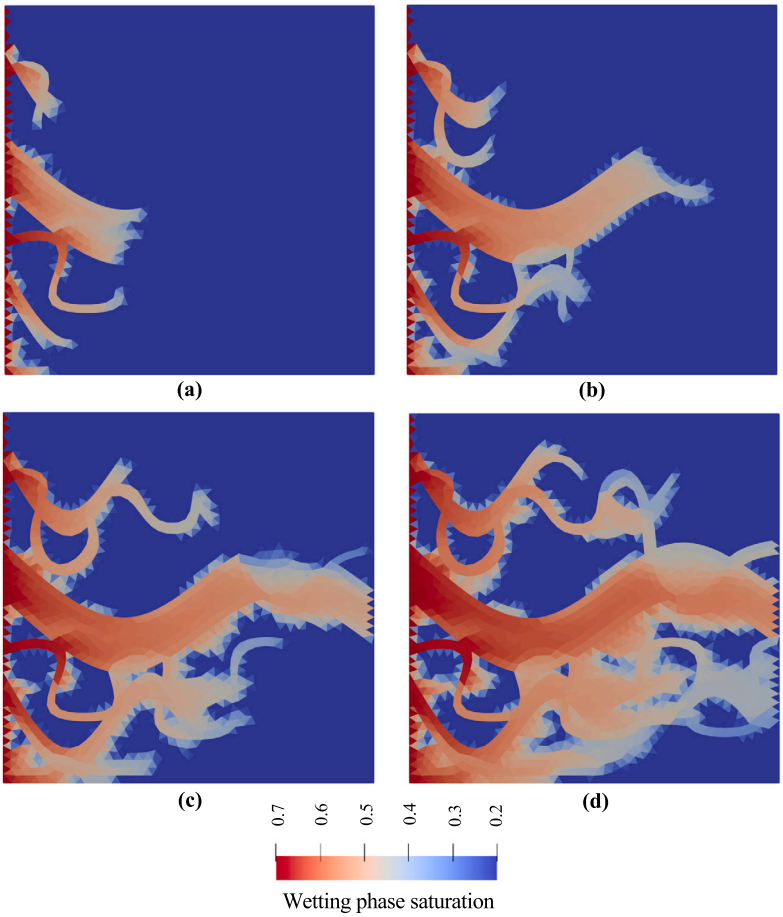

Fig. 15. The wetting phase saturation profile for experiment 4.5. The saturation solution before breakthrough in **(a)** and **(b)** with 0.03 and 0.07 PVI, respectively. The saturation solution after breakthrough in **(c)** and **(d)** with 0.11 and 0.16 PVI, respectively.

volumes from spanning subdomain boundaries. The approach is very efficient since it has similar DoF count to the CVFE and only introduces a small overhead to the computational requirements [4]. The computational overhead associated with using the HyCVFE method in comparison to the classical CVFE for numerical experiment 4.4 is 5%, 7%, and 11% for cases I, II, and III, respectively, while for numerical experiment 4.5 the HyCVFE method introduces about 11%.

The finite volume method using the two-point flux approximation (FV-TPFA) is well-suited for capturing cell-to-cell variability in material properties (e.g. [16]) on k-orthogonal grids. We compared the saturation solutions of FV-TPFA with the SM-CVFE to assess the robustness of FV-TPFA on the unstructured mesh shown in Fig. 16a that features variable element sizes and internal angle distributions, while exhibiting moderate permeability contrast between the background and the channel region. A snapshot of the saturation solution at 0.13 PVI for the SM-CVFE and the FV-TPFA is shown in Fig. 16b and 16c, respectively. Fig. 16d shows the L^{∞} norm of the relative error of the FV-TPFA saturation solution across all time steps with respect to the SM-CVFE solution. Large error values are observed for the FV-TPFA solution reaching up to 92%, indicating inaccuracies associated with the TPFA method. The limitations of FV-TPFA scheme on general, non-k-orthogonal grids were discussed in earlier work (e.g. [1,48,34]). The SM-CVFE combines the suitability of FV-TPFA to capture cell-to-cell variations in material properties, with the flexibility of CVFE methods for capturing accurate and stable flow field on arbitrary, unstructured and non-k-orthogonal, meshes.

We note that the benefits offered by the SM-CVFE approximation can extend beyond porous media flow problems. For example, the study of Hu et al. [29] applied the CVFE method to approximate the shallow water equations for an urban flooding model. Despite using a refined mesh where accuracy is needed, the model exhibited non-physical leakage along the boundaries separating the buildings from the surrounding region. The potential advantages offered by the SM-CVFE approach to model shallow water equations while eliminating the inconsistency of using the two-mesh approach are promising.

Future work

In our implementation of the SM-CVFE method, we used an IMPES-based approach to couple the flow and transport model for validation and testing of this new methodology. Ultimately, a fully implicit (FI) or a sequential fully implicit (SFI) (e.g. [32,33]) approximations are appropriate to overcome the CFL number limitation associated with explicit time stepping.

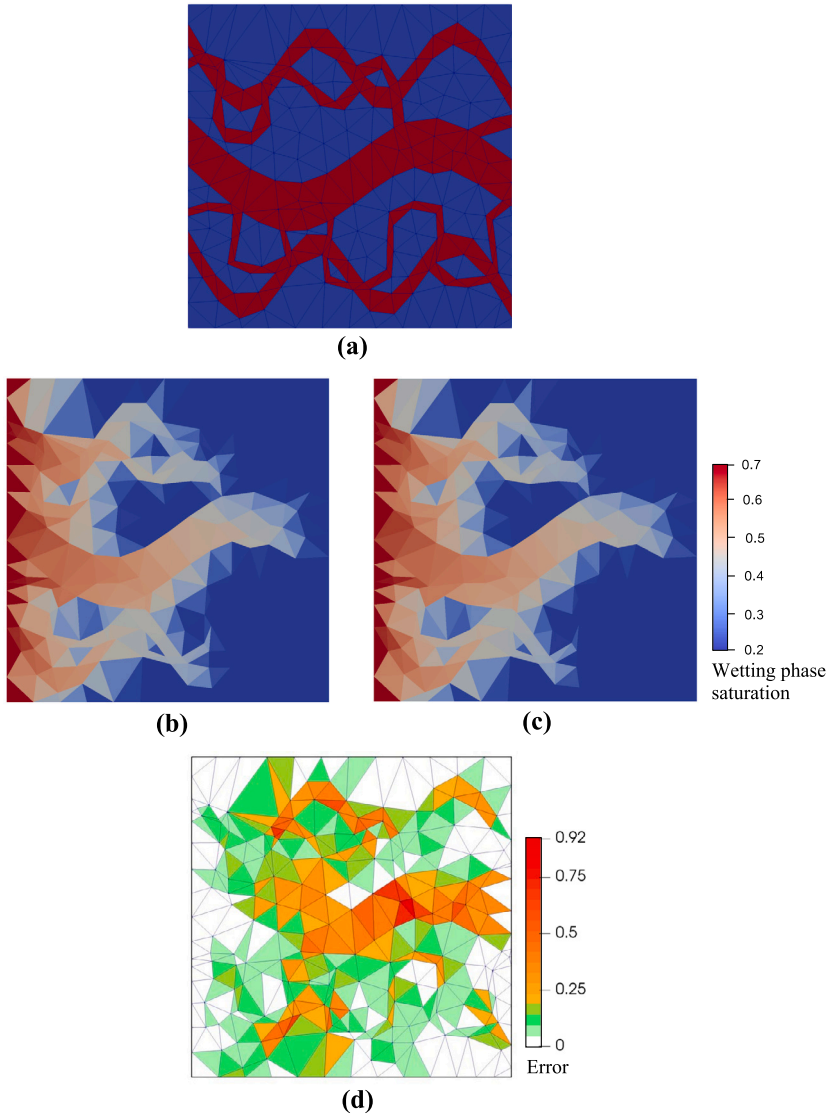

Fig. 16. (a) Model and mesh employed to compare the SM-CVFE and FV-TPFA saturation solutions, adapted from that used in experiment 4.5. The blue elements and red elements identify the low permeability background and high permeability channel regions, respectively, with an order of magnitude change in the permeability contrast between the regions. **(b)** The SM-CVFE saturation (reference) solution at 0.13 PVI. **(c)** The FV-TPFA saturation solution at 0.13 PVI. **(d)** L^{∞} norm of the relative saturation error for FV-TPFA scheme over all time steps.

Despite the general formulation described in Sections 3.2-3.3, the numerical experiments were established for 2D models. Demonstrations for 3D domains as well as implementation of parallel framework are essential for adopting this method to large scale and realistic subsurface models. The 3D implementation of the SM-CVFE approach has been tested and validated; the results will be subject of future work. For 3D models, we recommend employing tetrahedral elements, which offer flexibility in capturing the underlying geometry. The flow unknown discretization outlined in Section 3.1 is applied to tetrahedral elements with an element-wise pressure approximation and a linear velocity approximation. The fluxes between elements are then captured through triangular interfaces for tetrahedral elements, in contrast to line segments utilized in triangular elements, described in Section 3.6.

It is worth noting that the proposed SM-CVFE approach eliminates the dual control volume mesh which in return reduces the overall memory and CPU requirements. Both resources are often limited and can present a challenge to allocate while modeling large scale models. This has yet to be tested for 3D numerical experiments and compared to the classical approaches. Finally, the conditioning of the system assembled by the equations presents another challenge especially for modeling 3D domains. In our experience, realistic large-scale 3D models often suffer from poorly conditioned systems. The implications of the proposed SM-CVFE method on conditioning for 3D domains will be the subject for future work.

6. Conclusions

In this work, we presented a new discretization approach: the single mesh control volume finite element (SM-CVFE) method. The approach overcomes a well known challenge facing the family of CVFE methods by employing the element pair $P_{1,DG} - P_{0,DG}$ that requires a single, consistent mesh for the discretization of flow and transport variables. The computational requirements are comparable to the MFE methods; the SM-CVFE approach requires about 2.5 times the degrees of freedom (DoF) when compared to the CVFE method. The SM-CVFE approach establishes stable solutions that are mass conservative. We validated the approximation for single phase flow and two phase Buckley-Leverett model. Additionally, we presented several numerical experiments with challenging aspects including complex geometries and incorporated geostatistical models with strong heterogeneities. This work is first to show that the family of CVFE methods are suitable and efficient for modeling multiphase flow in the presence of element to element variations in the material properties. The presented SM-CVFE method offers a powerful framework that applies a consistent discretization and achieves accurate solutions while requiring a simple implementation that, in retrospect, seems quite natural. We believe that the SM-CVFE techniques put forth in this work provide interesting avenues for generalization and extension within and beyond the scope of porous media flow problems.

CRediT authorship contribution statement

Jumanah Al Kubaisy: Conceptualization, Methodology, Software, Validation, Visualization, Writing – original draft, Writing – review & editing. **Pablo Salinas:** Conceptualization, Methodology, Writing – review & editing. **Matthew D. Jackson:** Conceptualization, Methodology, Supervision, Writing – review & editing.

Declaration of competing interest

The authors declare that they have no known competing financial interests or personal relationships that could have appeared to influence the work reported in this paper.

Data availability

Data will be made available on request.

Acknowledgements

We thank Carl Jacquemyn for helpful discussions. Funding for Jumanah Al Kubaisy from Saudi Aramco is gratefully acknowledged.

References

[1] I. Aavatsmark, G.T. Eigestad, R.A. Klausen, M.F. Wheeler, I. Yotov, Convergence of a symmetric mpfa method on quadrilateral grids, Comput. Geosci. 11 (2007) 333–345, https://doi.org/10.1007/s10596-007-9056-8.

[2] A.S. Abushaikha, M.J. Blunt, O.R. Gosselin, C.C. Pain, M.D. Jackson, Interface control volume finite element method for modelling multi-phase fluid flow in highly heterogeneous and fractured reservoirs, J. Comput. Phys. 298 (2015) 41–61, https://doi.org/10.1016/j.jcp.2015.05.024, https://www.sciencedirect.com/science/article/pii/S0021999115003587.

[3] A.S. Abushaikha, K.M. Terekhov, A fully implicit mimetic finite difference scheme for general purpose subsurface reservoir simulation with full tensor permeability, J. Comput. Phys. 406 (2020) 109194, https://doi.org/10.1016/j.jcp.2019.109194, https://www.sciencedirect.com/science/article/pii/S002199911930899X.

[4] J. Al Kubaisy, P. Salinas, M.D. Jackson, A hybrid pressure approximation in the control volume finite element method for multiphase flow and transport in heterogeneous porous media, J. Comput. Phys. 475 (2023) 111839, https://doi.org/10.1016/j.jcp.2022.111839, https://www.sciencedirect.com/science/article/pii/S0021999122009020.

[5] K. Aziz, A. Settari, Petroleum Reservoir Simulation, Applied Science Publishers, 1979.

[6] P. Bastian, R. Helmig, Efficient fully-coupled solution techniques for two-phase flow in porous media: parallel multigrid solution and large scale computations, Adv. Water Resour. 23 (1999) 199–216, https://doi.org/10.1016/S0309-1708(99)00014-7, https://www.sciencedirect.com/science/article/pii/S0309170899000147.

[7] L. Bergamaschi, S. Mantica, G. Manzini, A mixed finite element–finite volume formulation of the black-oil model, SIAM J. Sci. Comput. 20 (1998) 970–997, https://doi.org/10.1137/S1064827595289303.

[8] F. Brezzi, D. Boffi, L. Demkowicz, R. Durán, R. Falk, M. Fortin, Mixed Finite Elements, Compatibility Conditions, and Applications, Springer, 2008, 2, 4–2.

[9] F. Brezzi, M. Fortin, Mixed and Hybrid Finite Element Methods, Springer, 1991.

[10] R.H. Brooks, A.T. Corey, Hydraulic properties of porous media and their relation to drainage design, Trans. ASABE 7 (1964) 26–0028.

[11] S. Buckley, M. Leverett, Mechanism of fluid displacement in sands, Trans. AIME 146 (1942) 107–116, https://doi.org/10.2118/942107-G, https://onepetro.org/TRANS/article-pdf/146/01/107/2177908/spe-942107-g.pdf.

[12] G. Chavent, G. Cohen, J. Jaffre, M. Dupuy, I. Ribera, Simulation of two-dimensional waterflooding by using mixed finite elements, Soc. Pet. Eng. J. 24 (1984) 382–390, https://doi.org/10.2118/10502-PA, https://onepetro.org/spejournal/article-pdf/24/04/382/2653226/spe-10502-pa.pdf.

[13] G. Chavent, G. Cohen, J. Jaffré, R. Eymard, D.R. Guérillot, L. Weill, Discontinuous and mixed finite elements for two-phase incompressible flow, SPE Reserv. Eng. 5 (1990) 567–575, https://doi.org/10.2118/16018-PA, https://onepetro.org/RE/article-pdf/5/04/567/2629131/spe-16018-pa.pdf.

[14] G. Chavent, J. Jaffre, Mathematical Models and Finite Elements in Reservoir Simulation, 1986.

[15] A.J. Chorin, Numerical solution of the Navier-Stokes equations, Math. Comput. 22 (1968) 745–762.

[16] M. Christie, M. Blunt, Tenth spe comparative solution project: a comparison of upscaling techniques, SPE Reserv. Eval. Eng. 4 (2001), https://doi.org/10.2118/66599-MS.

[17] P. Deveugle, M.D. Jackson, G. Hampson, M. Farrell, A. Sprague, J. Stewart, C. Calvert, Characterization of stratigraphic architecture and its impact on fluid flow in a fluvial-dominated deltaic reservoir analog: upper Cretaceous ferron sandstone member, Utah, AAPG Bull. 95 (2011) 693–727, https://doi.org/10.1306/09271010025.

[18] L.J. Durlofsky, A triangle based mixed finite element–finite volume technique for modeling two phase flow through porous media, J. Comput. Phys. 105 (1993) 252–266, https://doi.org/10.1006/jcph.1993.1072.

[19] L.J. Durlofsky, Accuracy of mixed and control volume finite element approximations to Darcy velocity and related quantities, Water Resour. Res. 30 (1994) 965–973, https://doi.org/10.1029/94WR00061, https://agupubs.onlinelibrary.wiley.com/doi/pdf/10.1029/94WR00061.

[20] M.G. Edwards, Unstructured, control-volume distributed, full-tensor finite-volume schemes with flow based grids, Comput. Geosci. 6 (2002) 433–452, https://doi.org/10.1023/A:1021243231313.

[21] L.S.K. Fung, A.D. Hiebert, L.X. Nghiem, Reservoir simulation with a control-volume finite-element method, SPE Reserv. Eng. 7 (1992) 349–357, https://doi.org/10.2118/21224-PA, https://onepetro.org/RE/article-pdf/7/03/349/2611950/spe-21224-pa.pdf.

[22] S. Geiger, S. Roberts, S.K. Matthäi, C. Zoppou, A. Burri, Combining finite element and finite volume methods for efficient multiphase flow simulations in highly heterogeneous and structurally complex geologic media, Geofluids 4 (2004) 284–299, https://doi.org/10.1111/j.1468-8123.2004.00093.x, https://onlinelibrary.wiley.com/doi/abs/10.1111/j.1468-8123.2004.00093.x.

[23] J.L.M.A. Gomes, D. Pavlidis, P. Salinas, Z. Xie, J.R. Percival, Y. Melnikova, C.C. Pain, M.D. Jackson, A force-balanced control volume finite element method for multi-phase porous media flow modelling, Int. J. Numer. Methods Fluids 83 (2017) 431–445, https://doi.org/10.1002/fld.4275, https://onlinelibrary.wiley.com/doi/abs/10.1002/fld.4275, https://onlinelibrary.wiley.com/doi/pdf/10.1002/fld.4275.

[24] G.H. Graham, M.D. Jackson, G.J. Hampson, Three-dimensional modeling of clinoforms in shallow-marine reservoirs: part 1. Concepts and application, AAPG Bull. 99 (2015) 1013–1047, https://doi.org/10.1306/01191513190, https://pubs.geoscienceworld.org/aapgbull/article-pdf/99/6/1013/3378809/BLTN13190.pdf.

[25] R. Helmig, R. Huber, Comparison of Galerkin-type discretization techniques for two-phase flow in heterogeneous porous media, Adv. Water Resour. 21 (1998) 697–711, https://doi.org/10.1016/S0309-1708(97)00023-7, https://www.sciencedirect.com/science/article/pii/S0309170897000237.

[26] R. Helmig, et al., Multiphase Flow and Transport Processes in the Subsurface: a Contribution to the Modeling of Hydrosystems, vol. 1, Springer, 1997.

[27] H. Hoteit, A. Firoozabadi, An efficient numerical model for incompressible two-phase flow in fractured media, Adv. Water Resour. 31 (2008) 891–905, https://doi.org/10.1016/j.advwatres.2008.02.004, https://www.sciencedirect.com/science/article/pii/S0309170808000353.

[28] H. Hoteit, R. Mosé, B. Philippe, P. Ackerer, J. Erhel, The maximum principle violations of the mixed-hybrid finite-element method applied to diffusion equations, Int. J. Numer. Methods Eng. 55 (2002) 1373–1390, https://doi.org/10.1002/nme.531, https://onlinelibrary.wiley.com/doi/pdf/10.1002/nme.531.

[29] R. Hu, F. Fang, P. Salinas, C. Pain, Unstructured mesh adaptivity for urban flooding modelling, J. Hydrol. 560 (2018) 354–363, https://doi.org/10.1016/j.jhydrol.2018.02.078, https://www.sciencedirect.com/science/article/pii/S0022169418301604.

[30] M.D. Jackson, G.J. Hampson, R.P. Sech, Three-dimensional modeling of a shoreface-shelf parasequence reservoir analog: part 2. Geologic controls on fluid flow and hydrocarbon recovery, AAPG Bull. 93 (2009) 1183–1208, https://doi.org/10.1306/05110908145, https://pubs.geoscienceworld.org/aapgbull/article-pdf/93/9/1183/3371177/bltn08145.pdf.

[31] M.D. Jackson, J.R. Percival, P. Mostaghimi, B.S. Tollit, D. Pavlidis, C.C. Pain, J.L. Gomes, A.H. El-Sheikh, P. Salinas, A.H. Muggeridge, M.J. Blunt, Reservoir modeling for flow simulation by use of surfaces, adaptive unstructured meshes, and an overlapping-control-volume finite-element method, SPE Reserv. Eval. Eng. 18 (2015) 115–132, https://doi.org/10.2118/163633-PA, https://onepetro.org/REE/article-pdf/18/02/115/2127830/spe-163633-pa.pdf.

[32] P. Jenny, S. Lee, H. Tchelepi, Adaptive fully implicit multi-scale finite-volume method for multi-phase flow and transport in heterogeneous porous media, J. Comput. Phys. 217 (2006) 627–641, https://doi.org/10.1016/j.jcp.2006.01.028, https://www.sciencedirect.com/science/article/pii/S002199910600026X.

[33] S.H. Lee, C. Wolfsteiner, H.A. Tchelepi, Multiscale finite-volume formulation for multiphase flow in porous media: black oil formulation of compressible, three-phase flow with gravity, Comput. Geosci. 12 (2008) 351–366, https://doi.org/10.1007/s10596-007-9069-3.

[34] K.A. Lie, An Introduction to Reservoir Simulation Using MATLAB/GNU Octave: User Guide for the MATLAB Reservoir Simulation Toolbox (MRST), Cambridge University Press, 2019.

[35] K. Lipnikov, G. Manzini, M. Shashkov, Mimetic finite difference method, J. Comput. Phys. 257 (2014) 1163–1227, https://doi.org/10.1016/j.jcp.2013.07.031, https://www.sciencedirect.com/science/article/pii/S0021999113005135, physics-compatible numerical methods.

[36] S.K. Matthäi, H.M. Nick, C. Pain, I. Neuweiler, Simulation of solute transport through fractured rock: a higher-order accurate finite-element finite-volume method permitting large time steps, Transp. Porous Media 83 (2010) 289–318, https://doi.org/10.1007/s11242-009-9440-z.

[37] S.K. Matthäi, A. Mezentsev, M. Belayneh, Finite element–node-centered finite-volume two-phase-flow experiments with fractured rock represented by unstructured hybrid-element meshes, SPE Reserv. Eval. Eng. 10 (2007) 740–756, https://doi.org/10.2118/93341-PA, https://onepetro.org/REE/article-pdf/10/06/740/2559431/spe-93341-pa.pdf.

[38] S. Nardean, M. Ferronato, A.S. Abushaikha, A novel block non-symmetric preconditioner for mixed-hybrid finite-element-based Darcy flow simulations, J. Comput. Phys. 442 (2021) 110513, https://doi.org/10.1016/j.jcp.2021.110513, https://www.sciencedirect.com/science/article/pii/S0021999121004083.

[39] R.A. Nelson, Geologic Analysis of Naturally Fractured Reservoirs, 2nd edition, Elsevier, 2001, https://app.knovel.com/hotlink/toc/id:kpGANFRE01/geologic-analysis-naturally/geologic-analysis-naturally.

[40] H. Nick, S. Matthäi, A hybrid finite-element finite-volume method with embedded discontinuities for solute transport in heterogeneous media, Vadose Zone J. 10 (2011) 299–312, https://doi.org/10.2136/vzj2010.0015, https://acsess.onlinelibrary.wiley.com/doi/abs/10.2136/vzj2010.0015.

[41] H.M. Nilsen, K.A.A. Lie, J.R. Natvig, Accurate modeling of faults by multipoint, mimetic, and mixed methods, SPE J. 17 (2012) 568–579, https://doi.org/10.2118/149690-PA, https://onepetro.org/SJ/article-pdf/17/02/568/2097674/spe-149690-pa.pdf.

[42] H. Osman, G.H. Graham, A. Moncorge, C. Jacquemyn, M.D. Jackson, Is cell-to-cell scale variability necessary in reservoir models?, Math. Geosci. 53 (2021) 571–596, https://doi.org/10.1007/s11004-020-09877-y.

[43] P. Salinas, D. Pavlidis, Z. Xie, H. Osman, C. Pain, M. Jackson, A discontinuous control volume finite element method for multi-phase flow in heterogeneous porous media, J. Comput. Phys. 352 (2018) 602–614, https://doi.org/10.1016/j.jcp.2017.09.058, https://www.sciencedirect.com/science/article/pii/S0021999117307313.

[44] K. Schmid, S. Geiger, K. Sorbie, Higher order fe–fv method on unstructured grids for transport and two-phase flow with variable viscosity in heterogeneous porous media, J. Comput. Phys. 241 (2013) 416–444, https://doi.org/10.1016/j.jcp.2012.12.017, https://www.sciencedirect.com/science/article/pii/S0021999112007486.

[45] J.R. Shewchuk, Delaunay refinement algorithms for triangular mesh generation, in: 16th ACM Symposium on Computational Geometry, Comput. Geom. 22 (2002) 21–74, https://doi.org/10.1016/S0925-7721(01)00047-5, https://www.sciencedirect.com/science/article/pii/S0925772101000475.

[46] R. Temam, Sur l'approximation de la solution des équations de Navier-Stokes par la méthode des pas fractionnaires (ii), Arch. Ration. Mech. Anal. 33 (1969) 377–385.

[47] L. Tran, J. Kim, S. Matthäi, Simulation of two-phase flow in porous media with sharp material discontinuities, Adv. Water Resour. 142 (2020) 103636, https://doi.org/10.1016/j.advwatres.2020.103636, https://www.sciencedirect.com/science/article/pii/S030917081931214X.

[48] X.H. Wu, R.R. Parashkevov, Effect of grid deviation on flow solutions, SPE J. 14 (2009) 67–77, https://doi.org/10.2118/92868-PA, https://onepetro.org/SJ/article-pdf/14/01/67/2549768/spe-92868-pa.pdf.

[49] A. Younes, P. Ackerer, F. Lehmann, A new mass lumping scheme for the mixed hybrid finite element method, Int. J. Numer. Methods Eng. 67 (2006) 89–107, https://doi.org/10.1002/nme.1628, https://onlinelibrary.wiley.com/doi/pdf/10.1002/nme.1628.

[50] N. Zhang, A.S. Abushaikha, An efficient mimetic finite difference method for multiphase flow in fractured reservoirs, in: SPE Europec Featured at EAGE Conference and Exhibition Day 2 Tue, June 04, 2019, 2019, https://onepetro.org/SPEEURO/proceedings-pdf/19EURO/2-19EURO/D021S001R011/1174632/spe-195512-ms.pdf.

[51] N. Zhang, A.S. Abushaikha, Fully implicit reservoir simulation using mimetic finite difference method in fractured carbonate reservoirs, in: SPE Reservoir Characterisation and Simulation Conference and Exhibition Day 2 Wed, September 18, 2019, 2019, https://onepetro.org/SPERCSC/proceedings-pdf/19RCSC/2-19RCSC/D021S010R003/1178790/spe-196711-ms.pdf.